PHYSICAL REVIEW B VOLUME 53, NUMBER 23 15 JUNE 1996-I

Electronic structure and physical properties of $NbSi_2$

V. N. Antonov, B. Yu. Yavorsky, and A. P. Shpak
Institute of Metal Physics, Kiev, Ukraine

Vl. N. Antonov and O. Jepsen
Max-Planck-Institut für Festkörperforschung, D-70569 Stuttgart, Federal Republic of Germany

G. Guizzetti and F. Marabelli
Istituto Nazionale di Fisica della Materia – Dipartimento di Fisica ''Alessandro Volta,''
Universitá degli Studi di Pavia, Via Bassi 6, I-27100 Pavia, Italy

(Received 6 July 1995)

We have investigated the optical properties of $NbSi_2$ experimentally and theoretically. The reflectivity and ellipsometry measurements were performed on single crystals with two light polarizations. From these the optical conductivity and the complex dielectric function were obtained from 0 to about 6 eV. The measured optical functions were compared with those calculated using local density functional theory and the linear muffin-tin orbital method. The calculated electronic structure is analyzed using orbital projected densities of states (DOS) and the optical functions are interpreted in terms of interband transitions. We, furthermore, compare the calculated DOS with previously measured x-ray photoemission spectra and bremsstrahlung isochromat spectra. We calculated some soft x-ray emission spectra and compared them with experiments. We find generally excellent agreement between theory and all experiments. [S0163-1829(96)05323-4]

I. INTRODUCTION

The current interest in transition-metal silicides (TMS) is due to their high-temperature stability, resistance to degradation, and high electrical conductivity, which make them suited as Schottky barriers, Ohmic contacts, and interface diffusion barriers in microelectronic devices.[1] In the last few years, extensive work on the electronic structure and physical properties of TMS has been performed.[2–6]

Some physical properties of $NbSi_2$ have been studied previously. The thermal expansion of the TMS in the groups IV–VII, which includes $NbSi_2$, have been investigated from room temperature to about 1500 K by x-ray powder-diffraction technique.[7] The electronic structure of various TMS has been studied in Ref. 8 by x-ray photoemission spectroscopy (XPS) and bremsstrahlung isochromat spectroscopy (BIS). The measurements were interpreted in terms of calculated density of states (DOS) and XPS and BIS matrix elements. The soft x-ray emission (SXE) spectrum of $NbSi_2$ was measured in Refs. 9 and 10. The transport properties in some single-crystalline disilicides, such as $TiSi_2$, VSi_2, $NbSi_2$, etc. were studied in Ref. 11. The low-temperature specific heat of $TiSi_2$, VSi_2, $NbSi_2$ were reported in Ref. 12. The resistivity and the magnetoresistance of these three compounds were studied in Refs. 13 and 14.

In this paper we present the optical spectra of $NbSi_2$ [the reflectivity $R(\omega)$, the conductivity $\sigma(\omega)$, and the real $\varepsilon_1(\omega)$, and imaginary $\varepsilon_2(\omega)$ parts of the dielectric function], obtained by reflectivity and ellipsometric measurements. We compare these with first-principles local density functional[15] (LDA) calculations using the linear muffin-tin orbital (LMTO) method in atomic-spheres approximation (LMTO-ASA).[16–18] The structures in the optical functions are interpreted in terms of interband transitions. We compare the calculated density of states with previous XPS and BIS measurements. We have finally calculated some SXE spectra and compare them with available experiments.

We find good detailed agreement between all these experiments and the calculated electronic structure, which leads us to the conclusion that the LDA gives a consistent picture of the electronic structure in $NbSi_2$.

II. EXPERIMENTS

A. Sample preparation and measurements

Single crystals of $NbSi_2$ were grown at the Laboratory des Materiaux et du Genie Physique in Grenoble using a modified Czochralski pulling technique from a levitated melt in a cold copper crucible (Hukin type). Details of the process are described elsewhere.[19]

Single-crystalline rods with a length of about 4 cm were obtained; from these rods, oriented slices were cut and then polished in order to obtain optically flat and shiny surfaces of about 1 cm^2.

Reflectivity (R) at near normal incidence with polarized light was measured over the spectral range from about 5 to 6 eV with two different spectrometers: a Fourier transform spectrometer model Bruker IFS 113v for the infrared [with grid polarizer on polyethylene and KRS5 for far infrared (FIR) and mid infrared (MIR), respectively] and a double monochromator spectrophotometer model Varian CARY 5 (with Polaroid polarizers) from 0.4 eV to the ultraviolet. The R spectra were taken using as a reference a gold and an aluminum mirror in the infrared and in the visible-UV parts of the spectrum, respectively. The relative R values were then normalized to the absolute reflectivity of the mirrors.

0163-1829/96/53(23)/15631(7)/$10.00

Moreover, spectroscopic ellipsometric (SE) measurements were performed in the energy range 1.4–5 eV with an instrument Sopra ESG4 at an incidence angle of 70°.

The results were obtained for light polarized parallel ($\|$) and perpendicular ($\perp$) to the crystallographic c axis. A small discrepancy of a few percent between R values obtained by photometry and those obtained by ellipsometry was probably due to the higher sensitivity of the reflectance to the scattering of light by macroscopic roughness of the surface with respect to the ellipsometry, which measures only relative intensities. The curves were then corrected at the highest energies by a small rigid shift in order to fit the ellipsometric results.

In the SE range, ε_1 and ε_2 were derived directly by inverting the ellipsometric functions $\tan(\psi)$ and $\cos(\Delta)$. For energies lower than 1.4 eV, ε_1 and ε_2 were obtained by Kramers-Kronig transform of the reflectivity data. For energies higher than 5 eV, we assumed R constant up to about 10 eV, and then decreasing as ω^{-s}, with $s \sim 5$. This ensured that $\tilde{\varepsilon}$ coincided with the ellipsometrically measured functions to within 0.5% from 1.4 to 5 eV.

At energies below 5 meV an extrapolation was obtained by the Hagens-Rubens relation $R = 1 - \sqrt{2\omega/\pi\sigma_{\text{dc}}}$, where the dc conductivity σ_{dc} was taken from the experiments of Guizzetti *et al.*[20]

B. Processing experimental data

The experimental reflectivities show metallic behavior for both polarizations, with high values at the lowest energies. The upper energy limit of this region is indicated by the cut-off of R at about 0.7 eV, corresponding, in principle, to the free carrier plasma resonance screened by the interband transitions. The latter dominate the second spectral region above 0.7 eV, where several structures appear.

Small bumps or smooth shoulders due to interband transitions are, however, present at low energies for $E \| c$.

As far as the intraband optical properties are concerned, we analyzed the FIR response by including a Drude term in the complex dielectric function

$$\tilde{\varepsilon}(\omega) = \varepsilon_1(\omega) + i\varepsilon_2(\omega) = \tilde{\varepsilon}_{\text{interband}}(\omega) - \frac{\omega_p^2}{\omega(\omega + i/\tau)}, \tag{1}$$

where $\omega_p = (4\pi N e^2/m^*)^{1/2}$ is the plasma frequency of the free carriers, with density N and effective mass m^*. τ is the scattering time related to the dc conductivity by $4\pi\sigma_{\text{dc}} = \omega_p^2 \tau$. Due to the contribution from interband transitions, which extends down to the lowest energies, $\tilde{\varepsilon}_{\text{interband}}$ cannot be considered constant even in this part of spectrum. The decomposition of the measured spectra into interband and intraband contributions is therefore quite difficult.

Using Eq. (1) and the experimentally determined σ_{dc},[20] we fitted the experimental reflectivity with the plasma frequency as a free parameter. By the fit $\tilde{\varepsilon}$ was deconvoluted into a Drude term and an interband term and the Kramers-Kronig consistency of the interband part was verified. The best fit for both polarizations yielded the values $\omega_{p\|} = 2.36 \pm 0.1$ eV and $\omega_{p\perp} = 1.85 \pm 0.1$ eV. The relatively large error associated with these values is due to the very high sensitivity of Kramers-Kronig analysis (and of the decomposition procedure) to the absolute value of the FIR reflectivity.

The ratio of plasma frequencies $(\omega_{p\|}/\omega_{p\perp})^2 \sim 1.6$ is in good agreement with the ratio of the resistivities at room temperature.[20] This ratio depends essentially on the effective masses along the two crystallographic directions.

In a model of one parabolic conduction band the two plasma frequencies can be expressed as $\omega_{p\|}^2 = 4\pi e^2 n/m_\|^*$ and $\omega_{p\perp}^2 = 4\pi e^2 n/m_\perp^*$. Within the same model the measured electronic contribution to the specific heat $\gamma = (k_B^2/3\hbar^2) m_\perp^* k_{F\|} = 3.4$ mJ/(mol K^2),[12] where k_F is the Fermi vector. From the three relations above one can obtain an estimate of the carrier density $n = k_{F\|}^3 (m_\perp^*/m_\|^*)/3\pi^2 = 4.73 \times 10^{21}$ cm^{-3}, and the effective masses $m_\|^* = 1.16 m_e$ and $m_\perp^* = 1.86 m_e$.

III. STRUCTURE AND COMPUTATION DETAILS

$NbSi_2$ crystallizes in the hexagonal $C40$ structure with the space group $P6_222(D_6^4)$ and three $NbSi_2$ formula units per primitive cell. It is nonsymmorphic with nonprimitive translations $\tau = (0,0,c/3)$ and $(0,0,2c/3)$, which interchange individual $NbSi_2$ layers. The arrangement of the individual atoms is illustrated in Fig. 1(a). The hexagonal Brillouin zone (BZ) is shown in Fig. 1(b), where the symmetry points and lines are labeled in accordance with the standard notation of Ref. 21. Although the D_6 point group contains only half of the full-hexagonal D_{6h} symmetry operations, the energy bands E_n^k exhibit full-hexagonal symmetry as a result of time-reversal symmetry.[22] The lattice constants are $a = 4.819$ Å and $c = 6.592$ Å.[23]

We have performed first-principles self-consistent (LDA)[15] calculations of the electronic structure using the LMTO-ASA method, including the so-called combined correction term.[16–18] A detailed description of the LMTO-ASA method, including its application to the electronic structure of compounds, has been given elsewhere.[24,25] We shall therefore only give some details of the calculations here. The calculations were semirelativistic, i.e., all relativistic effects were taken into account except for the spin-orbit coupling. The angular momentum expansion of the basis functions included $l = 3$ for niobium and $l = 2$ for silicon. The Nb f orbitals have a minor effect on the energy bands E_n^k, however, it is necessary to include them because usually the $d \rightarrow f$ oscillator strength is much larger than that for the $p \rightarrow d$ or $s \rightarrow p$ transitions. The k integrated functions were evaluated by the tetrahedron method[26] on a grid of 1183 k points in the irreducible part of the BZ [Fig. 1(b)]. From the energy bands and the LMTO eigenvectors, we calculated the total and orbital (l) projected DOS, the optical functions (R, σ, ε_1, and ε_2), and some SXE spectra.

IV. ENERGY BANDS AND DENSITY OF STATES

The energy band structure of $NbSi_2$, shown in Fig. 2, is rather complicated. It may, however, be understood from the total and partial DOS's presented in Fig. 3. The occupied part of the band structure can be divided into two regions separated by a pseudogap at about 6 eV below the Fermi energy. The bands in the lowest region have mostly Si s

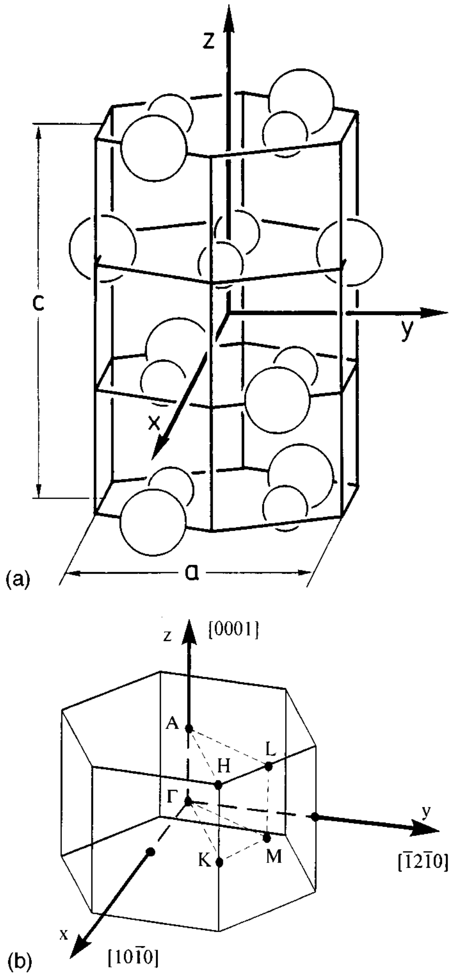

FIG. 1. Primitive unit cell for the hexagonal *C*40 structure of $NbSi_2$. Large spheres correspond to Nb atoms and small spheres correspond to silicon atoms. (b) The Brillouin zone for hexagonal $NbSi_2$.

character with some amount of Nb *sp* character mixed in. The highest region can be characterized as a bonding combination of Nb *d* and Si *p* states with some Nb *p* states mixed in. This complex is separated from the antibonding states by a second pseudogap around the Fermi level. There is a fair amount of Nb *sp* states and Si *s* states mixed into the antibonding states.

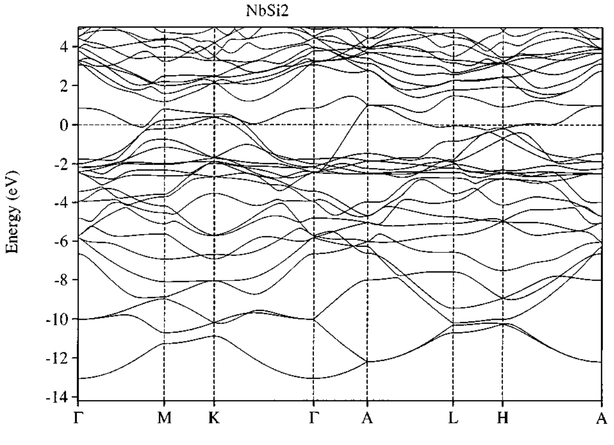

FIG. 2. Self-consistent energy band structure of $NbSi_2$ along some symmetry lines in the Brillouin zone shown in Fig. 1.

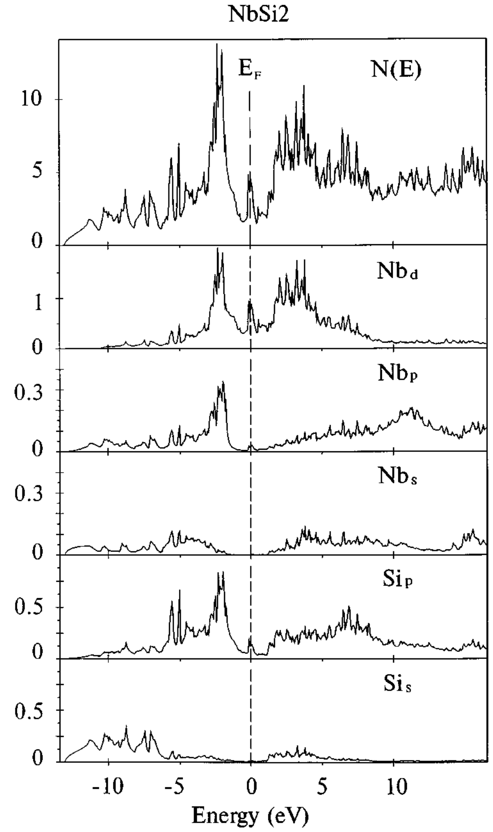

FIG. 3. Self-consistent total density of states $N(E)$ and Nb *s*, *p*, *d* and Si *s* and *p* partial densities of states. Units are states/(cell eV) or states/(atom eV).

In Fig. 4 our calculated DOS are compared with the experimental XPS and BIS spectra of Speier *et al.*[8] The calculated DOS were broadened to account for finite-lifetime effects and experimental resolution. The measured spectra may be seen to be described fairly well by our LDA calculations. The calculated DOS is smaller than the XPS at the bottom of the valence band, which has dominantly Si *s* character. This may be due to matrix element effects, which are neglected when comparing DOS with XPS.

V. CALCULATED OPTICAL PROPERTIES AND COMPARISON WITH EXPERIMENTAL DATA

The linear response of a system to an external electromagnetic field in the long-wavelength limit is determined by the imaginary part, $\varepsilon_2(\omega)$, of the complex dielectric function $\tilde{\varepsilon}$ [Eq. (1)]. We have calculated the dielectric function for frequencies well above those of the phonons and therefore only considered electronic excitations. We used the random phase approximation and neglected local-field and finite lifetime effects.[27] The dielectric function is a tensor. By an appropriate choice of the principal axes we can, however, diagonalize it, which allows us to consider only the diagonal matrix elements $\tilde{\varepsilon}^{\nu\nu}(\omega)$ with $\nu=x,y,z$. The interband contribution to the imaginary part of the dielectric function is given by

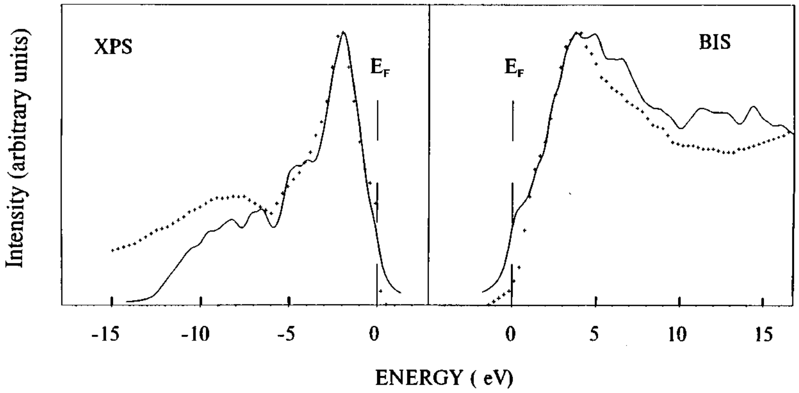

FIG. 4. Comparison between the calculated broadened DOS (full line) and the experimental XPS and BIS spectra from Ref. 8 (crosses) for $NbSi_2$.

$$\varepsilon_2^{\nu\nu}(\omega)=\frac{8\pi^2e^2}{m^2\omega^2}\sum_{n\neq n'}^{\text{unocc}}\sum_{n'}^{\text{occ}}\int_{\text{BZ}}|P_{nn'}^{\nu}(\mathbf{k})|^2 \times\delta(E_n^{\mathbf{k}}-E_{n'}^{\mathbf{k}}-\hbar\omega)\frac{d^3k}{(2\pi)^3}, \tag{2}$$

where $P_{nn'}^{\nu}(\mathbf{k})$ is the projection of the momentum matrix elements $P_{nn'}(\mathbf{k})$ along the ν direction of the electric field $\mathbf{E}$. $E_n^{\mathbf{k}}$ are the one-electron energies.

After having evaluated (2), we calculate the interband contribution to the real part of the dielectric function $\varepsilon_1(\omega)$ from the Kramers-Kronig relation:

$$\varepsilon_1(\omega)=1+\frac{2}{\pi}\text{P}\int\frac{\varepsilon_2(\omega')\omega'd\omega'}{\omega'^2-\omega^2}, \tag{3}$$

where P stands for the principal value. Finally, we add the intraband contribution to obtain the total complex dielectric function. We neglect this contribution to $\varepsilon_2(\omega)$ according to the perfect crystal approximation (the defects and lattice oscillations are absent). The intraband contribution to $\varepsilon_1(\omega)$ is given by

$$\varepsilon_1^{\nu\nu}(\omega)_{\text{intra}}=1-\frac{(\omega_p^{\nu\nu})^2}{\omega^2}, \tag{4}$$

where the squared plasma frequency is given by

$$(\omega_p^{\nu\nu})^2=\left(\frac{e}{\pi\hbar}\right)^2\sum_n\int_{\text{BZ}}d^3k[\partial E_n^{\mathbf{k}}/\partial k^{\nu}]^2\delta(E_n^{\mathbf{k}}-E_f). \tag{5}$$

We also calculated the optical conductivity and the reflectivity $R(\omega)$ using Eqs. (2)–(5) and the following relations:

$$\sigma(\omega)=\frac{\omega}{4\pi}\varepsilon_2(\omega) \tag{6}$$

and

$$R(\omega)=\left|\frac{\sqrt{\tilde{\varepsilon}}-1}{\sqrt{\tilde{\varepsilon}}+1}\right|^2. \tag{7}$$

We first calculate directly the imaginary part of dielectric function (2) in a wide energy range from 0 to 16 eV. The real part of the dielectric function and the other optical functions were then calculated using the formulas presented above. The calculated values of the plasma frequencies are $\omega_{p\parallel}=3.96$ eV and $\omega_{p\perp}=3.04$ eV, which are somewhat larger than those previously extracted by Drude analysis (2.36 ±0.1 and 1.85 ± 0.1 eV, respectively). The anisotropy in the plasma frequency gives rise to anisotropy of the optical properties in the infrared region. Figure 5 shows the optical conductivity of $NbSi_2$ for the two light polarizations $E\parallel c$ and $E\perp c$ in the energy range from 0 to 8 eV. There are six maxima in $\sigma(\omega)$, each of which originates from the same interband transitions for both polarizations. The difference in intensity for the two polarizations is due to the transition matrix element. A large anisotropy of the optical conductivity is found below about 2 eV. The strong peak (1) for the $E\perp c$ polarization at 0.4 eV originates from the superposition of two high-intensity partial contributions from the $19\rightarrow20$ and $20\rightarrow21$ interband transitions, i.e., transitions from just below the Fermi energy to just above it.

The $19\rightarrow20$ interband transitions take place in the vicinity of the symmetry point M and the symmetry directions $M-K$ and $\Gamma-K$ and the $20\rightarrow21$ interband transitions take place around the $\Gamma-M$ symmetry direction. The same peak may be seen for the other polarization, $E\parallel c$, but due to optical transition matrix elements the intensity is 5 times weaker. The second peak, which may be seen for the $E\parallel c$ polarization at 1.6 eV, is due to $19\rightarrow22$ interband transitions (i.e., transitions from just below the Fermi energy to about 1.5 eV above it) around the $M-K$ and $\Gamma-K$ symmetry directions. The corresponding interband transitions for the $E\perp c$ polarization is 8 times weaker and hardly visible in the figure. The shoulder at 1.2 eV in the $E\perp c$ polarization can be explained by $18\rightarrow21$ interband transitions, i.e., transitions from about 1 eV below the Fermi energy to just above it. The double peak, number three, comes from the $19\rightarrow22,23,24$ interband transitions (from just below the Fermi energy to

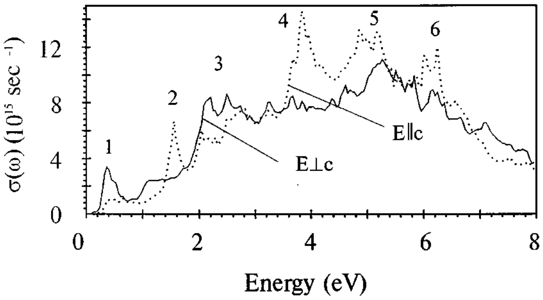

FIG. 5. The calculated optical conductivity of $NbSi_2$.

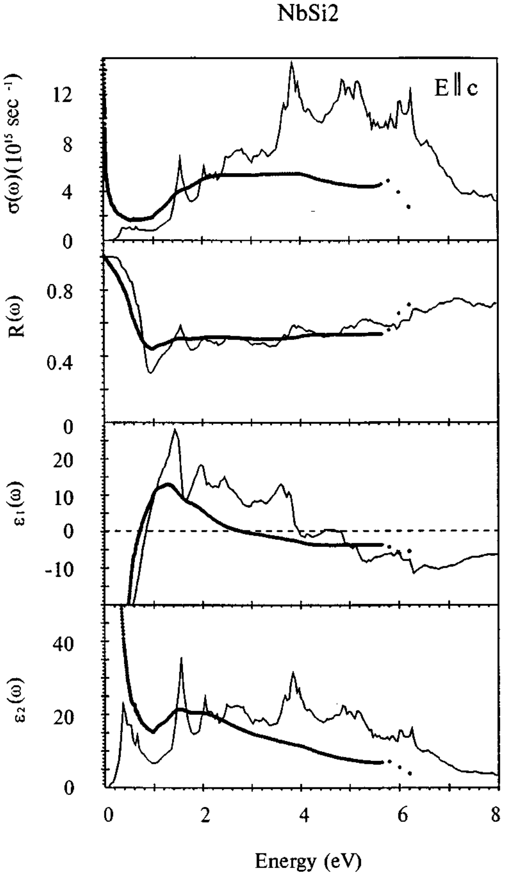

FIG. 6. Comparison between the experimental (circles) and calculated (solid line) optical conductivity $\sigma(\omega)$, reflectivity R, real part $\varepsilon_1(\omega)$, and imaginary part $\varepsilon_2(\omega)$ of the dielectric function of $NbSi_2$ for $\mathbf{E}\|c$.

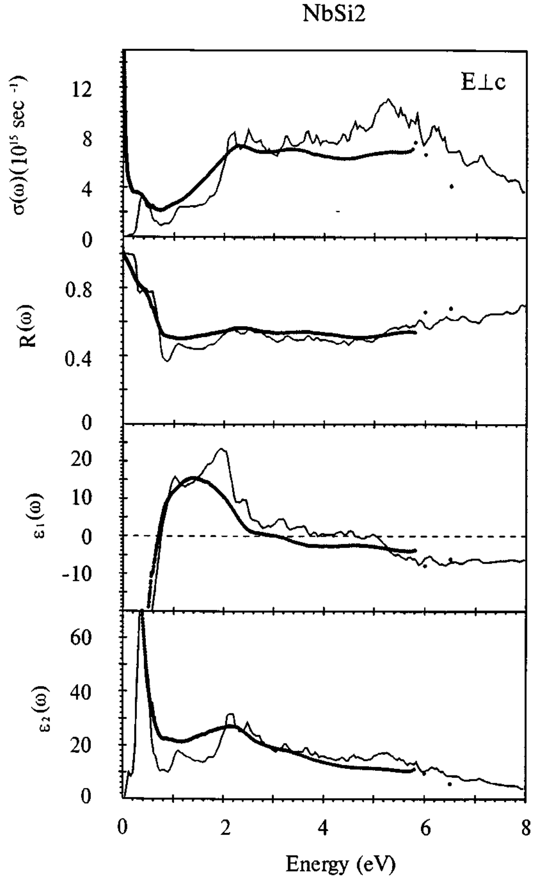

FIG. 7. Comparison between the experimental (circles or thick line) and calculated (solid line) optical conductivity $\sigma(\omega)$, optical reflectivity R, real part $\varepsilon_1(\omega)$, and imaginary part $\varepsilon_2(\omega)$ of the dielectric function of $NbSi_2$ for $\mathbf{E}\perp$ c.

about 2 eV above it) for both polarizations. The most intense 4th maximum in the $E\|c$ polarization at 4 eV is formed by the 12,13→25; 15,16→23; 16→24 and 18→27 interband transitions (from about 2 eV below the Fermi energy to about 2 eV above it) in an extended part of the BZ. The largest contribution comes from transitions between the 16th and the 23rd energy bands. The 5th double peak is formed from the 13,14→25,26; 14→28 and 18→28 interband transitions (from about 2 eV below the Fermi energy to about 3 eV above it) for both polarizations. The maximum number 6 is formed by 14,15→30 and 15→31 interband transitions, from about 2 eV below the Fermi energy to about 4 eV above it.

In Figs. 6 and 7 we compare the calculated optical conductivity $\sigma(\omega)$, the reflectivity $R(\omega)$, $\varepsilon_1(\omega)$, and $\varepsilon_2(\omega)$ with the experiments for the parallel and perpendicular polarization, respectively. As may be seen, theory and experiment agree in detail with each other for both polarizations.

We shall first discuss the results for the parallel polarization. In ε_2, the first peak shows up as a small kink in the experiments. In σ this peak becomes a shoulder, which in the experiments is hidden by the upturn of σ for small energies. The calculated peaks 2 to 4 are nicely seen at exactly the same energies in the measured ε_2 and σ. Peak number 6 is clearly seen in the experiments but the position of this as well as the edge slightly above it, is situated about 1 eV lower in the experimental curves. The reason for this may be that the final states for the transitions (band 30 and 31) are high above the Fermi energy and the reference energies for the linear expansion (the E_ν's) in the LMTO calculations were chosen at the center of gravity of the occupied bands. If the E_ν's had been chosen higher for the unoccupied states, the energies of these would have been lower.[17] Peak number 5 is not clearly seen in the experiments. This may be because it is hidden by the tail of the very strong 4th peak. Peaks 2 to 4 and 6 are also clearly present in the measured reflectivity.

For the perpendicular polarization, the strong 1st peak is very pronounced in the conductivity and the shoulder at about 1.2 eV is seen in both ε_2 and σ. The rest of the peaks are present in both functions. Since peak 4 is very weak for this polarization, peak 5 shows up clearly. As in the parallel polarization, all structures are found at the same energies in theory and experiments, except for the 6th peak and the high-energy edge. Again, better agreement for the latter could have been obtained by choosing the LMTO reference energies for the final states at higher energies. The same good agreement between theory and experiments is found for the reflectivity and for this even the very low energy 1st peak may be seen clearly.

It should be mentioned that the anisotropy of the optical functions in $NbSi_2$ in the energy range from 1 to 5 eV is not as strong as in WSi_2 (Ref. 2) and $PdSi_2$ (Ref. 3).

VI. SOFT X-RAY EMISSION SPECTRA

X-ray emission spectroscopy is one of the most efficient tools for studying the electronic structure of solids. In this experiment the energy distribution of emitted photons, created by valence electron – core hole combination, is measured. The experiment is therefore probing the symmetry (via the transition matrix elements) and the energy distribution of the valence states. Direct comparison between our one-electron theory and an experiment is, however, complicated by the finite width of the core hole due to many-body effects and the experimental resolution.

The intensity distribution is given by[28,29]

$$I(\omega)=\frac{\alpha^3\omega}{2\pi}\sum_{n\mathbf{k}}|\langle\Psi_c|e^{i\mathbf{q}\cdot\mathbf{r}}\cdot\mathbf{A}\cdot\mathbf{p}|\Psi_{n\mathbf{k}}\rangle|^2\delta(\hbar\omega-E_c+E_n^{\mathbf{k}}), \tag{8}$$

where $\alpha=e^2/\hbar c\approx 1/137$ is the fine-structure constant; Ψ_c, $\Psi_{n\mathbf{k}}$ and E_c, $E_n^{\mathbf{k}}$ are the wave functions and energies of the core and valence states, respectively; $\mathbf{p}$ is the electron momentum operator; $\mathbf{q}$ is the wave vector of a photon with the polarization vector $\mathbf{A}$. In the dipole approximation the x-ray emission intensity averaged over the polarizations of the emitted photon is given by

$$I(\omega)\propto\omega\sum_{n\mathbf{k}}|\langle\Psi_c|\nabla|\Psi_{n\mathbf{k}}\rangle|^2\delta(\hbar\omega-E_c+E_n^{\mathbf{k}}). \tag{9}$$

Using an angular momentum expansion for Ψ_c and $\Psi_{n\mathbf{k}}$, Eq. (9) can be reduced to the simple form[28,29]

$$I_l(E)=w[f_{l,l-1}(E)N_{l-1}(E)+f_{l,l+1}(E)N_{l+1}(E)], \tag{10}$$

where $N_l(E)$ is the l projected DOS and $f_{l,l'}(E)$ is an effective dipole matrix element.[28–30] Therefore, the intensity distribution factorizes into partial DOS's modulated by transition probabilities.

Some theoretical [using Eq. (10) above] and experimental x-ray emission spectra of NbSi_2 are compared in Fig. 8. The calculated spectra have been broadened to mimic the finite width of the core levels and the experimental resolution. The Nb L_{III} emission spectrum is determined by the $d\rightarrow 2p_{3/2}$ and $s\rightarrow 2p_{3/2}$ transitions. The contribution from the s states is only about 2%. The Nb L_{III} emission spectrum is smooth and slightly asymmetric. The lack of fine structure is due to a considerable width of the $2p$ core level, which smears out all the peaks in the partial d DOS. There is, however, a structure around -4.5 eV in the theoretical curve corresponding to a shoulder in the d DOS (Fig. 3). The corresponding structure is seen clearly in the theoretical and experimental XPS spectrum (Fig. 4).

The Nb M_{V} emission spectrum is mostly determined by $p\rightarrow 3d_{5/2}$ transitions. The contribution from the f states is only about 2%. There are four structures in the theoretical spectrum (1–4) and three in the experiments (3–5). The structures 3 and 4 are reproduced well in the calculations although the intensity of the third structure is somewhat smaller. The theoretical curve has two low-energy structures (1 and 2), which are not observed experimentally. The shape of experimental M_{V} spectrum is distorted by a strong inner line M_ζ ($M_{\mathrm{IV,V}}\rightarrow M_{\mathrm{II,III}}$), which is superimposed on the low-energy part. The experimentally observed fifth structure, occurring above the Fermi energy, is associated with the M_{IV} emission spectrum ($p\rightarrow 3d_{3/2}$ transitions).

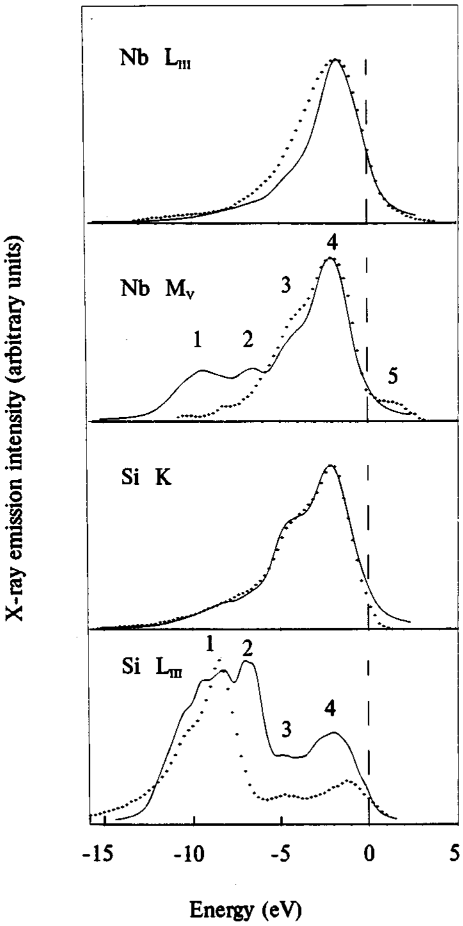

FIG. 8. Comparison between the experimental (dots) and the theoretical (full line) SXE spectra of NbSi_2. The experiments are from Ref. 9.

The best agreement between theory and experiment is obtained for the Si K spectrum, which is dominated by $p\rightarrow s$ transitions. The two strong structures in the Si p DOS (Fig. 3) at -5 and -2 eV appear as two clear peaks in the XSE spectrum.

The Si L_{III} spectrum consists of four structures, labeled 1–4 in Fig. 8, and they are due to the transitions $s\rightarrow 2p_{3/2}$ and $d\rightarrow 2p_{3/2}$. The structures 1 and 2 are predominant transitions from the s states, while the 3rd and 4th structures are mixed s and d transitions. Structure 1 has three peaks in the calculated spectrum, of which only two are seen in the experiments. The second structure is not clearly seen in the experiments, but the 3rd and 4th peaks agree well in theory and experiments.

VII. CONCLUSION

We have presented reflectivity and ellipsometry measurements on high-quality single crystals and LDA calculations with the LMTO method of the reflectivity, the optical conductivity, and the complex dielectric function of hexagonal

$NbSi_2$ in a wide energy range and for light polarizations parallel and perpendicular to the crystallographic c axis. We found excellent agreement between measurements and the LDA theory. We have explained the structures in the measured spectra in terms of interband transitions. We found some anisotropy in the optical functions below 2 eV and between 4 and 5 eV, the spectra were, however, much more isotropic than the spectra from other transition metal silicides. We have, furthermore, compared our DOS with XPS and BIS measurements and the calculated soft x-ray emission spectra with previous measurements and found that they agree very well.

ACKNOWLEDGMENTS

We are grateful to Dr. U. Gottlieb and Professor R. Madar at the Ecole Nationale Supérieure in Grenoble for making their high-quality single-crystalline samples available to us and to Dr. J. Gräfenstein for having read the manuscript carefully. One of us (V.N.A.) would like to thank the MPI-FKF for hospitality during his stay in Stuttgart. This work was supported by the European Community program: Human Capital and Mobility through Contract No. CHRX-CT93-0318, and the International Science Foundations: Support for Basic Sciences in the former Soviet Union (G. Soros Foundation) Grant No. U42200.

---

[1] K.N. Tu and J.W. Mayer, in *Thin Films Interdiffusion and Interactions*, edited by J.M. Poate, K.N. Tu, and J.W. Mayer (Wiley, New York, 1978).

[2] V.N. Antonov, Vl.N. Antonov, O. Jepsen, O.K. Andersen, A. Borghesi, C. Bosio, F. Marabelli, A. Piaggi, G. Guizzetti, and F. Nava, Phys. Rev. B **44**, 8437 (1991).

[3] M. Amiotti, G. Guizzetti, F. Marabelli, A. Piaggi, V.N. Antonov, Vl.N. Antonov, O. Jepsen, O.K. Andersen, A. Borghesi, F. Nava, V.V. Nemoshkalenko, R. Madar, and A. Rouault, Phys. Rev. B **45**, 13 285 (1992).

[4] V. Bellani, G. Guizzetti, F. Marabelli, A. Piaggi, A. Borgesi, F. Nava, V.N. Antonov, Vl.N. Antonov, O. Jepsen, O.K. Andersen, and V.V. Nemoshkalenko, Phys. Rev. B **46**, 9380 (1992)

[5] V.N. Antonov, B.Yu. Yavorsky, V.V. Nemoshkalenko, Vl.N. Antonov, O. Jepsen, O.K. Andersen, E.G. Haanapel, M. Vosgerau, W. Joss, P. Wyder, R. Madar, and A. Rouault, Phys. Rev. B **49**, 17 022 (1994).

[6] O.K. Andersen, O. Jepsen, Vl.N. Antonov, V.N. Antonov, B.Yu. Yavorsky, A.Ya. Perlov, and A.P. Shpak, Physica B **204**, 65 (1995).

[7] I. Engstrom and B. Lonnberg, J. Appl. Phys. **63**, 4476 (1981).

[8] W. Speier, L. Kumar, D.D. Sarma, R.A. de Groot, and J.C. Fuggle, J. Phys. Condens. Matter **1**, 9117 (1989).

[9] V.V. Nemoshkalenko, A.P. Shpak, V.P. Krivitsky, L.I. Nikolaev, and L.M. Yupko, Phys. Metals Metallurgy **40**, 1191 (1976).

[10] A.S. Shulakov, T.M. Zimkina, V.A. Fomichev, and V.S. Neshpor, in *Solid State Physics: Advances in Research and Applications*, edited by H. Ehrenreich *et al.* (Academic, New York, 1974), Vol. 16, p. 401.

[11] F. Nava, E. Mazzega, M. Michelini, O. Laborde, O. Thomas, J. P. Senateur, and R. Madar, J. Appl. Phys. **65**, 1584 (1989).

[12] J.C. Lasjaunias, O. Laborde, and U. Gottlieb, J. Low Temp. Phys. **92**, 335 (1993).

[13] U. Gottlieb, O. Laborde, O. Thomas, F. Weiss, A. Rouault, J.P. Senateur, and R. Madar, Surf. Coat. Technol. **45**, 237 (1991).

[14] U. Gottlieb, O. Laborde, O. Tomas, A. Rouault, J. P. Senateur, and R. Madar, Appl. Surf. Sci. **53**, 247 (1991).

[15] U. von Barth and L. Hedin, J. Phys. C **4**, 2064 (1971).

[16] O.K. Andersen and O. Jepsen, Phys. Rev. Lett. **53**, 2571 (1984); O.K. Andersen, Z. Pawlowska, and O. Jepsen, Phys. Rev. B **34**, 5253 (1986).

[17] O.K. Andersen, O. Jepsen, and D. Glötzel, in *Highlights of Condensed-Matter Theory*, edited by F. Bassani, F. Fumi, and M.P. Tosi (North-Holland, New York, 1985).

[18] W.R.L. Lambrecht and O.K. Andersen, Phys. Rev. B **34**, 3439 (1986); O.K. Andersen, T. Paxton, O. Jepsen, and M. van Schilfgaarde (unpublished).

[19] O. Thomas, J.P. Senateur, R. Madar, O. Laborde, and E. Rosencher, Solid State Commun. **55**, 629 (1985).

[20] G. Guizzetti, F. Marabelli, A. Borgesi, F. Nava, U. Gottlieb, and O. Laborde, Appl. Surf. Sci. **73**, 237 (1993).

[21] C.J. Bradley and A.P. Cracknell, *The Mathematical Theory of Symmetry in Solids* (Clarendon, Oxford, 1972).

[22] M. Lax, *Symmetry Principles in Solid State and Molecular Physics* (Wiley, New York, 1974).

[23] R. Kubiak, R. Horyn, H. Broda, K. Lukaszewich, Bull. Acad. Pol. Sci. Ser. Sci. Chim. **20**, 429 (1972).

[24] O.K. Andersen, Phys. Rev. B **12**, 3060 (1975).

[25] H.L. Skriver, *The LMTO Method* (Springer, Berlin, 1984).

[26] O. Jepsen and O.K. Andersen, Solid State Commun. **9**, 1763 (1971).

[27] H. Ehrenreich and M.H. Cohen, Phys. Rev. **115**, 786 (1959).

[28] V.V. Nemoshkalenko, V.N. Antonov, Vl.N. Antonov, W. John, H. Wonn, and P. Ziesche, Phys. Status Solidi B **111**, 11 (1982).

[29] V.V. Nemoshkalenko and V.N. Antonov, *The Computational Methods of Physics in the Solid State Theory* (Naukova Dumka, Kiev, 1985).

[30] J. Kudrnovsky, L. Smrchka, and B. Velicky, Czech. J. Phys. B **25**, 785 (1975).